Computationally restoring the potency of a clinical antibody against SARS-CoV-2 Omicron subvariants

Thomas A. Desautels[1], Kathryn T. Arrildt[2], Adam T. Zemla[3], Edmond Y. Lau[2], Fangqiang Zhu[2], Dante Ricci[2], Stephanie Cronin[7], Seth J. Zost, Elad Binshtein[7], Suzanne M. Scheaffer[8], Taylor B. Engdahl[7], Elaine Chen[7], John W. Goforth[3], Denis Vashchenko[4], Sam Nguyen[1*], Dina R. Weilhammer[2], Jacky Kai-Yin Lo[2], Bonnee Rubinfeld[2], Edwin A. Saada[2], Tracy Weisenberger[2], Tek-Hyung Lee[2], Bradley Whitener[8], James B. Case[8], Alexander Ladd[1], Mary S. Silva[3], Rebecca M. Haluska[4], Emilia A. Grzesiak[3], Thomas W. Bates[5], Brenden K. Petersen[1], Larissa B. Thackray[8], Brent W. Segelke[2], Antonietta Maria Lillo[11], Shivshankar Sundaram[6], Michael S. Diamond[8,9,10], James E. Crowe, Jr.[7,12], Robert H. Carnahan[7,12], Daniel M. Faissol[1]

Computational Engineering Division[1], Biosciences and Biotechnology Division[2], Global Security Computing Applications Division[3], Applications Simulations and Quality Division[4], Global Security Directorate[5], Center for Bioengineering [6], Lawrence Livermore National Laboratory, Livermore, CA 94550, USA.

Vanderbilt Vaccine Center, Nashville, TN 37232, USA[7]

Departments of Medicine[8], Molecular Microbiology[9], Pathology & Immunology[10], Washington University School of Medicine, St. Louis, MO 63110, USA.

Los Alamos National Laboratory, Bioscience Division, Los Alamos, NM 87545, USA [11].

Department of Pediatrics, Vanderbilt University Medical Center, Nashville, TN 37232, USA[12].

*: Now Google, Mountain View, CA, 94043, USA

ABSTRACT

The COVID-19 pandemic has highlighted how viral variants that escape monoclonal antibodies can limit options to control an outbreak. With the emergence of the SARS-CoV-2 Omicron variant, many clinically used antibody drug products lost *in vitro* and *in vivo* potency, including AZD7442 and its constituent, AZD1061 [VanBlargan2022, Case2022]. Rapidly modifying such antibodies to restore efficacy to emerging variants is a compelling mitigation strategy. We therefore sought to computationally design an antibody that restores neutralization of BA.1 and BA.1.1 while simultaneously maintaining efficacy against SARS-CoV-2 B.1.617.2 (Delta), beginning from COV2-2130, the progenitor of AZD1061. Here we describe COV2-2130 derivatives that achieve this goal and provide a proof-of-concept for rapid antibody adaptation addressing escape variants. Our best antibody achieves potent and broad neutralization of BA.1, BA.1.1, BA.2, BA.2.12.1, BA.4, BA.5, and BA.5.5 Omicron subvariants, where the parental COV2-2130 suffers significant potency losses. This antibody also maintains potency against Delta and WA1/2020 strains and provides protection *in vivo* against the strains we tested, WA1/2020, BA.1.1, and BA.5. Because our design approach is computational—driven by high-performance computing-enabled simulation, machine learning, structural bioinformatics and multi-objective optimization algorithms—it can rapidly propose redesigned antibody candidates aiming to broadly target multiple escape variants and virus mutations known or predicted to enable escape.

Introduction:

In December 2019, the first cases of COVID-19 disease, caused by the novel coronavirus SARS-CoV-2, were reported in Wuhan, China. By February 2020, the virus had reached every populated continent. The global death toll for COVID-19 exceeded 6 million people within two years [WHO2020]. Worldwide spread of COVID-19 is attributed to efficient respiratory viral shedding and person-to-person transmission from both symptomatic and asymptomatic individuals [Wolfel2020,Bai2020]. Despite increasingly available vaccines and antibody treatments, the pandemic continues in part due to mutations in the virus, resulting in variants of concern (VOCs) that can escape existing vaccines and antibody drugs. Most notably, the Omicron variant (BA.1), first reported in South Africa in November 2021, outcompeted all other VOCs worldwide within weeks [Viana2022]. BA.1 contains over 50 mutations, 15 in the spike protein receptor binding domain (RBD), the primary target for therapeutic and prophylactic antibodies. These mutations reduce or eliminate the efficacy of most approved prophylactic and therapeutic antibodies [VanBlargan2022,Iketani2022,Wang2022].

For example, the prophylactic antibody combination tixagevimab + cilgavimab (Evusheld^{TM}), deployed under an emergency use authorization, exhibited potent *in vitro* neutralization activity against ancestral SARS-CoV-2 (Wuhan-1) and earlier VOCs (i.e., Delta (B.1.617.2)), but demonstrated reduced activity against Omicron BA.1 and the closely related BA.1.1. Tixagevimab + cilgavimab is composed of modified versions of the non-competing, neutralizing antibodies COV2-2196 and COV2-2130, both isolated from the B cells of convalescent patients exposed to SARS-CoV-2 in Wuhan, China in December 2019 [Zost2020, Dong2021]. COV2-2196 and COV2-2130 exhibit an approximately 10- to 100-fold reduction in neutralizing potency against Omicron BA.1 compared to previous virus variants, as did the two-component combination [VanBlargan2022, Cameroni2022]. COV2-2130 suffers an even greater,

1,000-fold loss in neutralization potency against Omicron BA.1.1 as compared to strains earlier in the pandemic [Wang2022, Tuekprakhon2022, Takashita2022].

Computational re-design is a promising strategy to recover antibody function and to avoid the time-consuming process of discovering entirely new therapeutic antibodies. Specifically, we introduce a small number of mutations to an escaped but regulatory-approved antibody product or clinically relevant congener, and virtually assess improvement to binding efficacy. We developed and used a computationally-driven approach, called Generative Unconstrained Intelligent Drug Engineering (GUIDE). This approach combines high-performance computing resources, simulation, and machine learning to co-optimize binding efficacy against multiple antigen targets, such as RBDs from several SARS-CoV-2 strains, along with other desirable attributes such as thermostability. The design process starts from structural models of the parental antibody in complex with one or more antigen targets. Importantly, the computational platform operates in a "zero-shot" setting, *i.e.*, designs are created without iteration through, or input from, wet laboratory experiments on proposed antibody candidates, relatives, or other derivatives of the parental antibody (*e.g.*, single-point mutants). While more challenging, such design approaches can scale with available computational resources and address many targets with dynamic freedom that is substantially greater than current wet laboratory methods.

Using over five million CPU (central processing unit) and GPU (graphics processing unit) hours over a 3-week period, we used our computational platform to execute repair of COV2-2130 and propose antibody candidates. From these proposed antibodies, we selected 376 antibody sequences for experimental validation.

Computational design

Our computationally-driven antibody design platform leverages simulation and machine learning to generate mutant antibody sequences that are co-optimized for multiple critical properties, without requiring experimental feedback (**Fig. 1**). The platform comprises three phases: problem formulation, computational design and selection of mutant antibody candidates, and experimental validation of proposed candidates.

We formulate a problem by identifying a parental antibody (in this case, COV2-2130) [Zost2020], a set of particular target antigens (the receptor binding domain or RBDs from spike proteins of VOCs Omicron BA.1, BA.1.1, and Delta), and corresponding co-structures. Here, we sought simultaneous binding improvements against Omicron BA.1 and BA.1.1 while maintaining binding to the Delta variant. We used co-structures that were both experimentally determined and computationally estimated, starting from co-structures including the wild-type antigen [Dong2021]. Since an experimental structure of the Omicron RBD was not available at the onset of our design process, we estimated the structure of the complex of the RBD with COV2-2130 using template-based structural modeling [zemla2005]. We incorporated experimentally determined Omicron RBD structures [mannar2022] into the design process as they became available. We considered more than twenty paratope residues for mutation, primarily in or near the heavy (H) or light (L) chain complementarity determining regions (CDRs; [selaculang2013]) H2, H3, L1, and L2, resulting in a search space containing approximately 10^{27} possible mutant sequences.

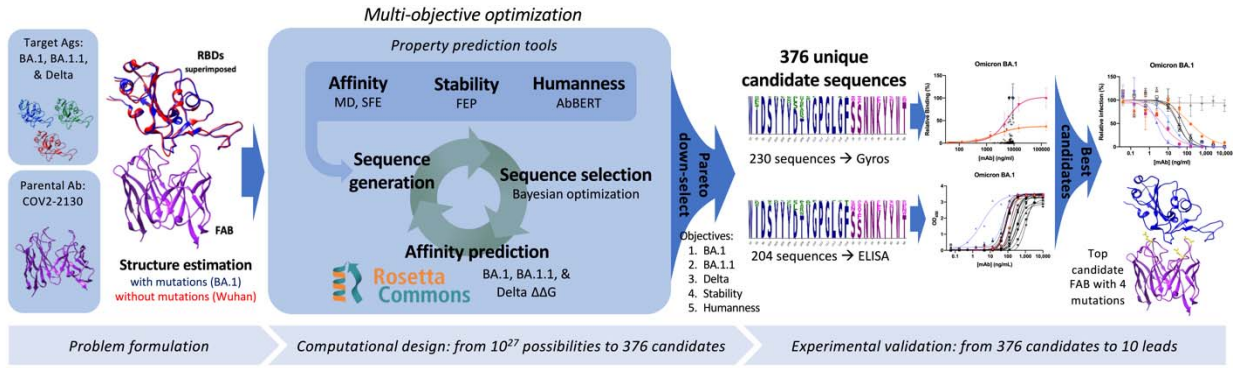

Figure 1. **Overview of the GUIDE computationally driven drug engineering platform.** Given target antigens and a parental antibody, co-structures are estimated experimentally and/or computationally (left). Within the main computational loop (center left), a sequence generator proposes multi-point mutant antibody candidates, and a Bayesian optimization agent selects which proposed sequences to evaluate via a set of affinity prediction tools. A subset of 376 computationally evaluated sequences based on Pareto optimality were experimentally evaluated for binding affinity by Gyros or ELISA (center right). The top 10 sequences are then evaluated for neutralization of SARS-CoV-2 variants (right). See Methods for details.

Our computational design approach was implemented as a multi-objective optimization problem defined over this large space of mutations to COV2-2130 paratope residues. We simultaneously considered five critical antibody properties: (1) binding affinity to Omicron BA.1 RBD, (2) binding affinity to BA.1.1 RBD, (3) binding affinity to Delta RBD, (4) thermostability, and (5) humanness (see below). We expected restored affinity to each RBD variant to result in restored neutralization because COV2-2130 competes with human angiotensin converting enzyme (ACE2) in SARS-CoV-2 spike binding [Zost2020]. Three complementary computational tools enable affinity prediction: atomistic potential of mean force molecular dynamics simulations, Structural Fluctuation Estimation (SFE) [zemla2022], and Rosetta Flex [barlow2018]. We estimated thermal stability using the Free Energy Perturbation (FEP) method [zhu2022].

Humanness was quantified as the log likelihood of each sequence, as estimated using the AbBERT model [Vashchenko22], a deep language model trained on a large database of human antibody sequences [Olsen2022]. If natural human sequences are assumed to be fit, avoiding statistically atypical sequences may limit pitfalls, particularly autoreactivity and poor expression. We used these tools to initialize a *sequence generator*, which proposes multi-residue mutations to the amino acid sequence of COV2-2130, biased toward residues that perform well across these critical properties. Within the optimization loop, this generator proposes batches of mutant antibody sequences. Next, we employed distributed software agents, each using *Bayesian optimization* or rules-based methods, to select a subset of promising candidate sequences to simulate in Rosetta Flex, yielding predicted binding affinities. Over the course of less than three weeks, spanning more than 4,000,000 CPU-hours and 1,000,000 GPU-hours, we computationally evaluated more than 125,000 antibody candidates.

From the outputs of these tools and other descriptors, such as the number of mutations in a proposed sequence, we calculated the Pareto optimal set [ehrgott2005] of thousands of sequences; this is the set of “non-dominated” sequences in the chosen computational fitness criteria, i.e., those for which there does not exist another sequence that is superior in all criteria. Finally, we chose 376 antibody designs for synthesis that balanced the diversity of selected sequences with constraints on experimental capacity.

Experimental evaluation:

Antibody and antigen production

We experimentally validated the designed candidates. To take advantage of available resources, we split our candidates into two partially overlapping subsets (1 and 2). Set 1 consisted of 230 designs expressed as IgG in HEK-293 cells (ATUM) and Set 2 consisted of 204 designs expressed as IgG via a pVVC-mCisK_hG1 vector (Twist BioScience) in transiently transfected CHO cells. Omicron antigens were produced in Expi293F cells (ThermoFisher Scientific) and purified on HisTrap Excel columns (Cytiva).

In the following experiments, we selected antigens or viral strains to determine if we had achieved three goals. These were our primary design goal of addressing BA.1 and BA.1.1; our secondary goal of maintaining efficacy against historical strains, where design explicitly targeted Delta but experiments often substituted WA1/2020 D614G; and our tertiary goal of determining whether our designs were robust to emerging VOCs.

Computationally designed antibodies maintained favorable expression yields

Because *in silico* derivatization of antibody sequences can inadvertently compromise production yield, we measured concentrations of the first cohort of 230 COV2-2130-derived recombinant antibodies produced and compared them to the parental antibody. The purified concentrations of 73.9% of re-designed antibodies exceeded that of the parental COV2-2130 antibody (170/230 mAbs at >171.2 mg/L), reaching as high as 305 mg/L. Only approximately 10% of designed antibodies gave poor yields relative to the parental molecule (22/230 mAbs at <135 mg/L, i.e.

80% of parental antibody yield). Our designs thus yielded candidates for downstream characterization that retained fundamental production properties of the parental antibody.

Computationally designed antibodies improved binding to Omicron subvariants and preserved thermostability

We screened all designed antibodies for binding by a single-concentration immunoassay (Gyrolab xPlore) in the contexts of BA.1, BA.1.1, and wild type RBDs (set 1; see **Fig. ED1** for later optimization of this assay) or a multi-concentration immunoassay (ELISA; **Fig. ED2**), respectively, in the context of wild type, BA.1 or BA.1.1 RBDs (set 2). In the single-concentration case, this value was chosen as a single dilution factor causing most designed antibody samples to fall in the dynamic range of the positive control. In both cases, we compared with a broadly cross-reactive control antibody S309 [pinto2020] and the parental COV2-2130 antibody. As intended, most antibody designs had altered binding profiles, i.e., the designed mutations were consequential. Thus, only approximately 11% of the first set of 230 designs retained wild-type WA1/2020 antigen binding at the measured concentration; roughly 6% improved binding against BA.1 and 5% against BA.1.1. Following this initial screen, we down-selected both sets of antibody designs to those with improved binding to Omicron subvariants BA.1 and BA.1.1.

These down-selected antibodies were remanufactured at larger scale. We characterized the resulting IgG antibodies by immunoassay and thermal shift (melt temperature) assessments. Seven of the eight top-performing antibodies preserved comparable binding to wild type (WA1/2020) and Delta RBDs and improved over the parental COV2-2130 antibody in their binding to Omicron BA.1 and BA.1.1 RBDs (**Fig. 2**). Furthermore, seven of the eight antibodies

had melting temperatures and expression properties comparable to those of COV2-2130. One antibody, 2130-1-0114-111 had reduced melting temperature. (**Table EDT1**). Antibody 2130-1-0114-112 displayed best-in-class binding across all RBD variants and had no significant difference in thermal stability compared to the parental COV2-2130 antibody.

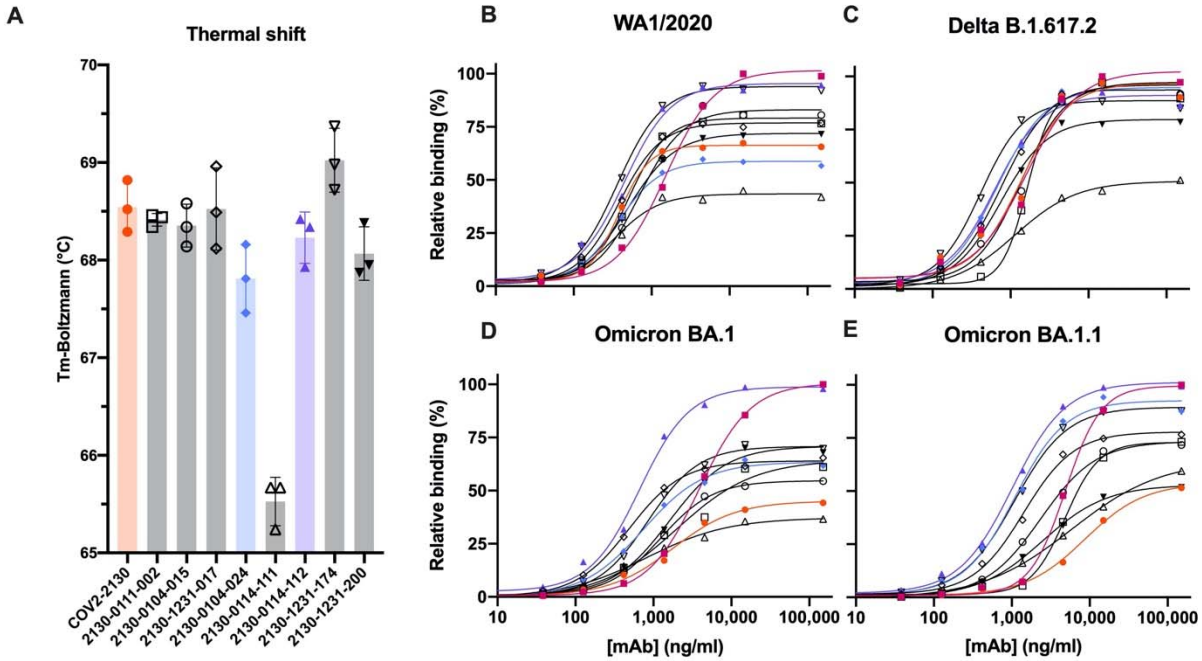

Figure 2. Computationally designed IgG antibodies improve Omicron binding and maintain parental thermostability and binding to historical strains. (A) The parental COV2-2130 (orange circles) and computationally designed antibodies (2130-1-0114-112 highlighted in purple ; remainder in black) were assayed for thermal shift (n=3, technical replicates). Bars indicate the mean and error bars indicate standard deviation. (B-E) The parental COV2-2130 antibody and computationally designed antibodies (represented by the same symbols as in A) and cross-reactive positive control antibody S309 (magenta squares) were analyzed for relative binding against four SARS-CoV-2 Spike-RBD variants in Gyrolab immunoassay: wild type WA1/2020 (B), Delta (C), Omicron BA.1 (D) and Omicron BA.1.1 (E). Lines represent 4-parameter logistic regression model fit using GraphPad Prism to each titration, executed without technical replicates.

Computationally designed antibodies restored neutralization to Omicron subvariants in pseudoviral neutralization assays

We performed pseudovirus neutralization assays to characterize the functional performance of selected antibody designs (**Fig. 3**). Our designs maintained neutralization activity against pseudoviruses displaying historical spike proteins (WA1/2020 D614G) and also achieved neutralization of those with Omicron BA.1 spikes. The single best candidate design, 2130-1-0114-112 , restored potent neutralization in the context of BA.1.1 and showed a two-order-of-magnitude improvement in IC50 vs. parental COV2-2130 for BA.1 and BA.4. These pseudovirus neutralization test results showed that our designs neutralized BA.2 and BA.4 more potently than COV2-2130, despite the emergence of these VOCs after the conception of our designs. We additionally tested 2130-1-0114-112's performance against BA.2.75, BA.4.6, which contain an R346T mutation, among others, and an artificially-constructed BA.2.75 + R346T, which matches the RBD sequence of BA.2.76 (**Fig. ED3**). 2130-1-0114-112 outperforms COV2-2130, including maintaining potent neutralization of BA.2.75 (IC50 of 2.6 ng/ml), which reduces COV2-2130's potency by more than 30-fold, and measurably neutralizes BA.4.6 and BA.2.75 + R346T, which are not effectively inhibited by COV2-2130.

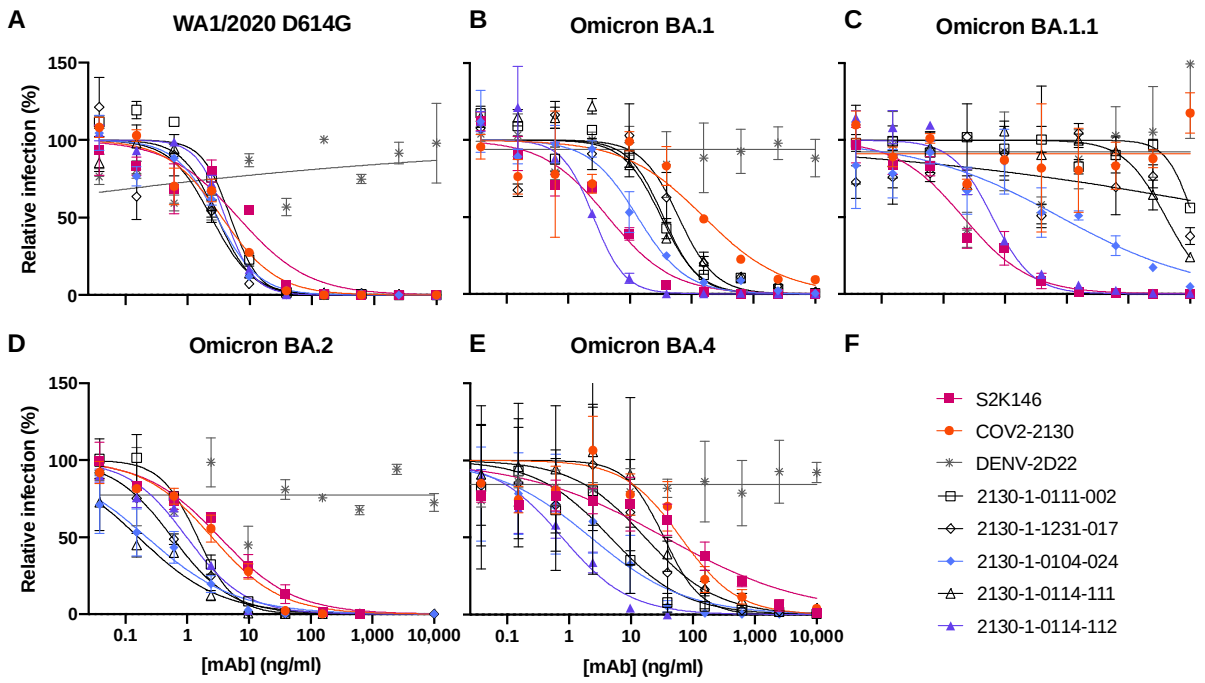

G

IC50 (ng/mL)	D614G	BA.1	BA.1.1	BA.2	BA.4
rDENV-2D22	NC	NC	>	NC	>
rS2K146	6.562	4.375	2.092	3.358	36.01
rCOV2-2130	3.595	157.5	NC	2.525	64.31
2130-1-0111-002	4.92	34.8	>	1.47	4.689
2130-1-1231-017	2.43	61.26	>	0.5686	17.06
2130-1-0104-024	2.986	13.25	78.46	0.2201	2.267
2130-1-0114-111	3.023	32	4027	0.1616	34.27
2130-1-0114-112	4.081	2.56	6.249	0.9845	0.7787

Figure 3: Designed antibodies improve pseudoviral neutralization over COV2-2130. The parental COV2-2130 antibody (orange circles), cross-reactive positive control antibody S2K146 (magenta squares), and down-selected computationally designed antibodies were assayed by neutralization with lentiviruses pseudotyped with spike variants of WA1/2020 D614G (A), Omicron BA.1 (B), BA.1.1 (C), BA.2 (D), and BA.4 (E). (G) IC50 values. ">" indicates a value > 10,000; NC indicates positive hill slope or failure to converge. Symbols indicate the mean and standard deviation of two technical replicates; curves are 4-parameter logistic regression models fit using GraphPad Prism.

Top computationally designed antibody, 2130-1-0114-112, *restores neutralization of Omicron subvariants in an authentic virus assay*

We evaluated our best antibody, 2130-1-0114-112 (four mutations, GH112E, SL32A, SL33A, TL59E), for authentic virus neutralization performance against several strains of SARS-CoV-2 by focus reduction neutralization test (FRNT) in Vero-TMPRSS2 cells (**Fig. 4**). These strains track the history of the pandemic, the early Omicron targets against which we designed, and subsequent strains of interest. The tested strains were WA1/2020 D614G, Delta (B.1.617.2), BA.1, BA.1.1, BA.2, BA.2.12.1, BA.4, BA.5, and BA.5.5. In all cases apart from Delta, 2130-1-0114-112 had an IC50 < 10 ng/mL. Compared to the parental COV2-2130, 2130-1-0114-112 restored potent neutralization activity against BA.1 and BA.1.1, showed a more than 5-fold improvement in IC50 against BA.2 and BA.2.12.1, and conferred 50-fold or greater improvements in IC50 against BA.4, BA.5, and BA.5.5. We also evaluated 2130-1-0114-112 and a less-mutated alternative design, 2130-1-0104-024 (SL32W, TL59E), in plaque assays with Vero E6-TMPRSS2-T2A-ACE2 cells (**Fig. ED4**). IC50 values for 2130-1-0104-024 were 37.7 ng/ml, 75.94 ng/ml and 781.7 ng/ml for Delta, BA.1, and BA.1.1 viruses, respectively.

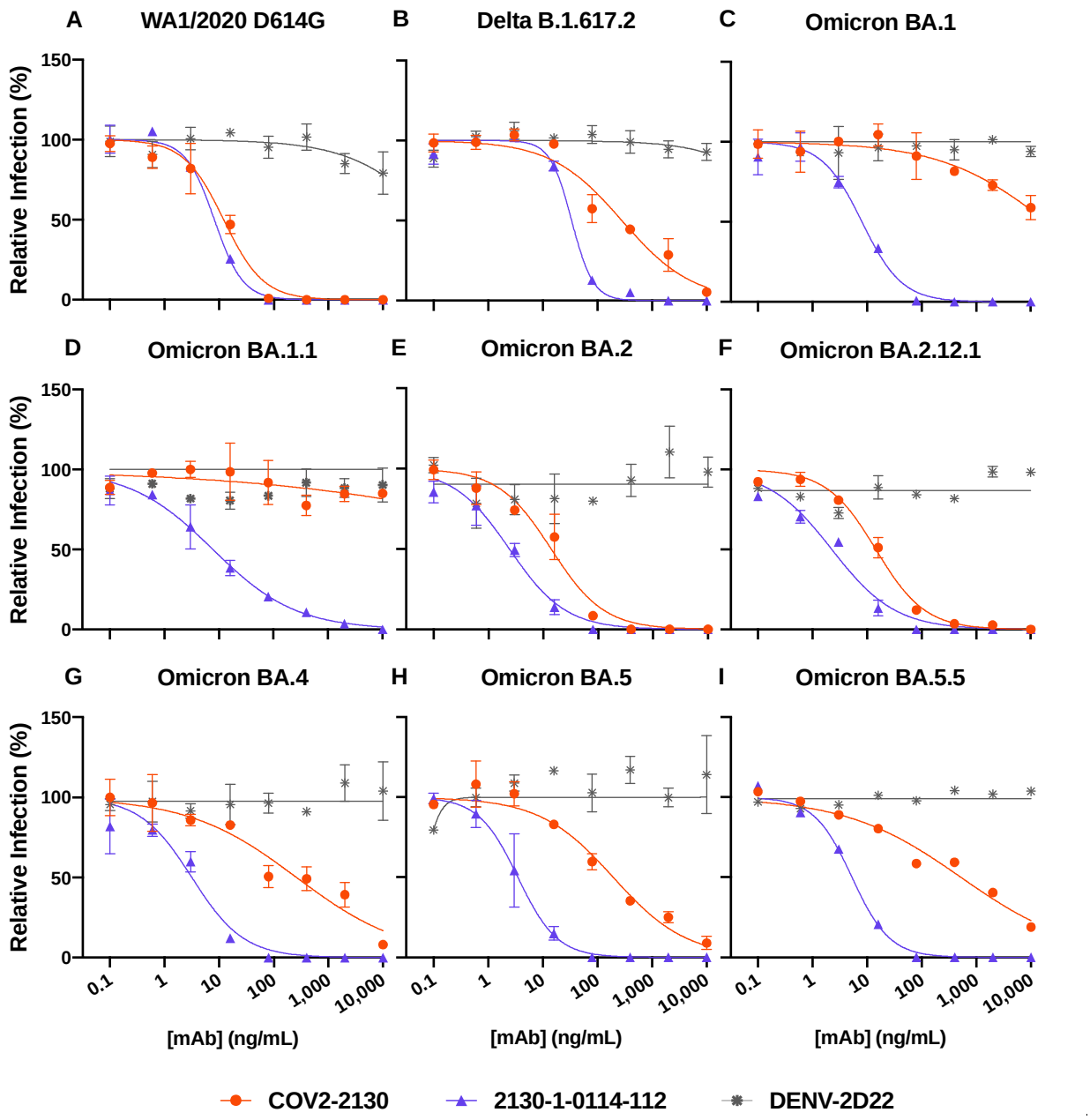

J

IC50 (ng/mL)	D614G	B.1.6.17.2	BA.1	BA.1.1	BA.2	BA.2.12.1	BA.4	BA.5	BA.5.5
2130 WT	12.11	282.5	>	>	13.88	14.56	261	195.6	522.1
2130-1-0114-112	8.186	33.94	8.079	7.766	2.404	2.268	3.163	3.514	5.287
rDENV-2D22	>	>	NC	NC	NC	NC	NC	NC	NC

Figure 4: 2130-1-0114-112 is potent in focus reduction neutralization tests with authentic virus in Vero-TMPRSS2 cells. 2130-1-0114-112 potently neutralizes (A) WA1/2020 D614G (B) Delta B.1.617.2, (C) Omicron BA.1, (D) Omicron BA.1.1, (E) Omicron BA.2, (F) Omicron BA.2.12.1, (G)

Omicron BA.4, (H) Omicron BA.5, and (I) Omicron BA.5.5 authentic viruses in focus reduction neutralization assays in Vero-TMPRSS2 cells. Experiments were performed in two technical replicates, symbols represent the mean of the duplicates, and fits are four-parameter logistic curves to the normalized data. (J) IC50 values corresponding to (A)-(I). ">" indicates IC50 values > 10,000; "NC" indicates fits that were unconverged, unstable, or with positive hill slope. Analyses were performed in GraphPad Prism.

Prophylaxis with 2130-1-0114-112 *protects against SARS-CoV-2 variants.*

To assess the comparative prophylactic efficacy of 2130-1-0114-112 and the parental COV2-2130 mAb *in vivo*, we administered to K18-hACE2 transgenic mice a single 100 μg (~5 mg/kg total) dose one day prior to intranasal inoculation with WA1/2020 D614G, BA.1.1, or BA.5 (88 mice in total, 9-10 for each mAb and viral strain). Although Omicron lineage viruses are less pathogenic in mice, they replicate efficiently in the lungs of K18-hACE2 mice [Case2022][Halfmann2022][Uraki2022][Ying2022]. Viral RNA levels were measured at 4 days post-infection in the nasal washes, nasal turbinates, and lungs (**Fig. 5**). As expected, the parental COV2-2130 mAb effectively reduced WA1/2020 D614G infection in the lungs (180,930-fold), nasal turbinates (42-fold) and nasal washes (25-fold) compared to the isotype control mAb. However, the COV2-2130 mAb lost protective activity against BA.1.1 in all respiratory tract tissue, whereas against BA.5, protection was maintained in the lungs (13,622-fold) but not in the nasal turbinates or nasal washes. In comparison, 2130-1-0114-112 protected against lung infection by WA1/2020 D614G (399,945-fold reduction), BA.1.1 (53,468-fold reduction), and BA.5 (160,133-fold reduction) compared to the isotype control mAb (**Fig. 5**). Moreover, in the upper respiratory tract (nasal turbinates and washes), 2130-1-0114-112 also conferred protection

against WA1/2020 D614G, BA.1.1, and BA.5. The differences in protection between the parental COV2-2130 and derivative 2130-1-0114-112 mAbs were most apparent in mice infected with BA.1.1, which directly parallels the neutralization data (**Fig. 3 and 4**).

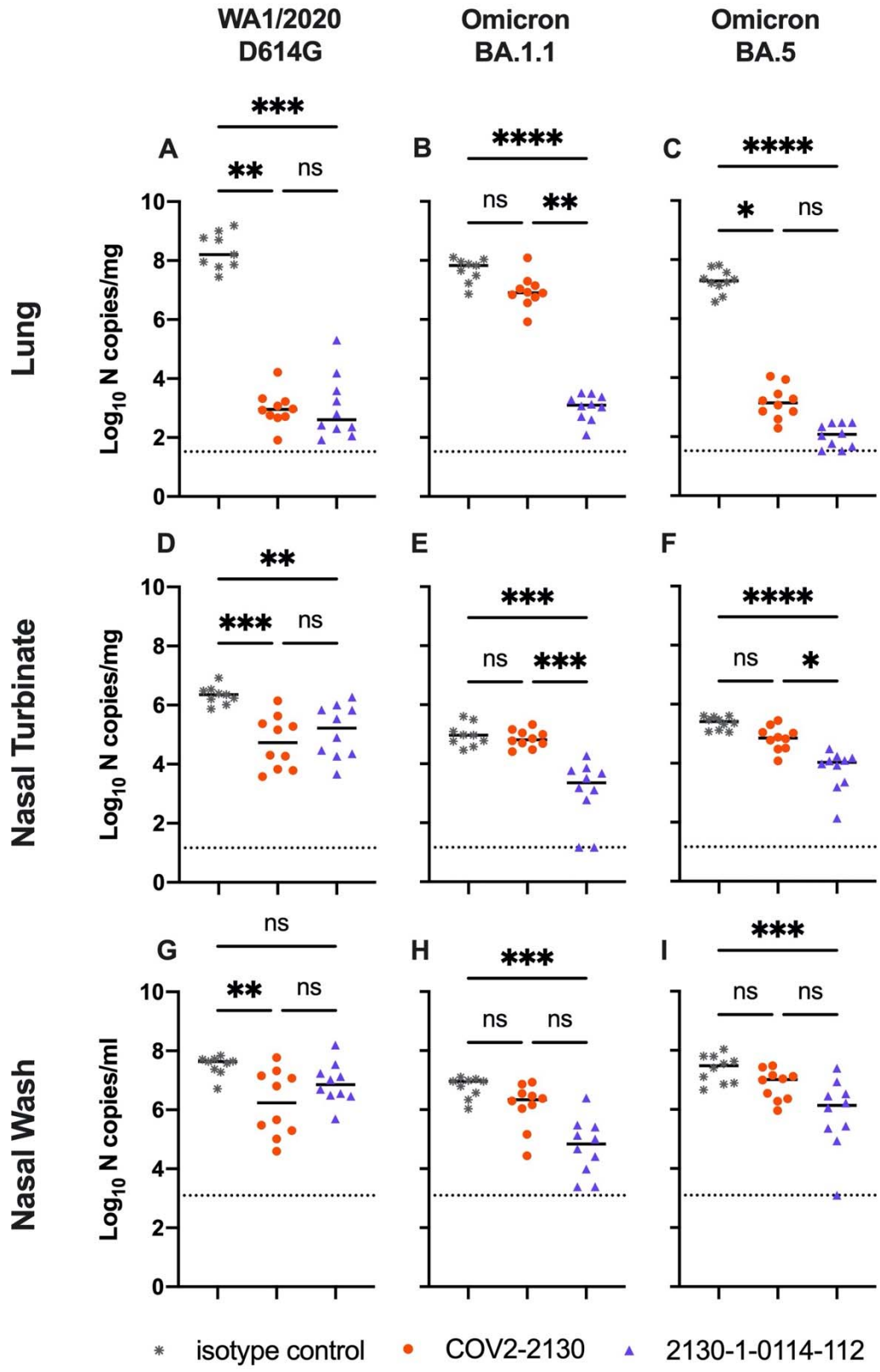

Figure 5: 2130-1-0114-112 provides *in vivo* prophylatic protection against SARS-CoV-2 variants.

Eight-week-old female K18-hACE2 mice were administered 100 μg (about 5 mg/kg) of the indicated mAb treatment by intraperitoneal injection one day before intranasal inoculation with 10^4 FFU of WA1/2020 D614G (Left), Omicron BA.1.1 (Center) or BA.5 (Right). Tissues were collected four days after inoculation, and viral RNA levels in the lungs (Top), nasal turbinates (Center), and nasal washes (Bottom) were determined by RT-qPCR (lines indicate median ± SEM.; n = 9 (WA1/2020 D614G and BA.1.1 isotype control groups) or 10 (all others) mice per group, two experiments; Kruskal-Wallis ANOVA with Dunn's multiple comparisons post-test; ns, not significant; *P < 0.05, **P < 0.01, ***P < 0.001, ****P < 0.0001). All analyses conducted in GraphPad Prism.

Structural basis for the restored potency of 2130-1-0114-112

To understand the molecular mechanism and the atomic details of the recognition of Omicron RBD by 2130-1-0114-112, we performed 3D reconstructions by cryo-electron microscopy (cryo-EM) of 2130-1-0114-112 in complex with the SARS-CoV-2 Omicron BA.2 spike at 3.26Å. Although the overall resolution was sufficient for model building, the interface region between the RBD and 2130-1-0114-112 was not well-resolved due to its flexibility. To address this issue, we performed focused refinement of this portion of the structure to ~3.6Å (EMD-28198, EMD-28199, PDB 8EDK) (**Fig. 6** and **Fig. ED6**, **Table EDT2**). This model shows the binding interface of 2130-1-0114-112/RBD and elucidates how 2130-1-0114-112 regains neutralization potency against Omicron VOCs. COV2-2130 forms extensive interactions with the RBD through HCDR2 and HCDR3, as well as LCDR1 and LCDR2 [Dong2021]. The interaction of these loops includes hydrogen bond networks and hydrophobic interactions. SARS-CoV-2 Omicron BA.2 has two mutations in close proximity to (7Å distance) COV2-2130 (N440K and Q498R) (**Fig. ED5A**). To improve binding interactions with Omicron subvariants, 2130-1-0114-112 modifies

three CDR loops (HCDR3, LCDR1, and LCDR2). The N440K mutation is on the edge of the RBD interface with the 2130-1-0114-112 HCDR3 loop and does not make direct contact with G112E. However, the mutation N440K introduces a positive charge to a local environment that has substantial hydrophobic-to-hydrophobic contact. The negative charge introduced by the G112E substitution (**Fig. 6C, D**) on the HCDR3 loop might improve the electrostatic interactions in this region. Although the structural resolution is not sufficient for modeling water molecules, it is possible that E112 and K440 could coordinate a water molecule. The local environment around the LCDR1 loop is mostly hydrophobic (comprised of RBD residues L452, F490 and L492, as well as the Omicron mutation E484A) with an N34 hydrogen bond (**Fig. 6D**). The hydrophilic-to-hydrophobic LCDR1 mutations introduced in 2130-1-0114-112, S32A and S33A, may favor the local environment and strengthen hydrophobic interactions with the RBD (**Fig. 6C, E**). Lastly, the T59E mutation in the LCDR2 loop establishes a new salt bridge with the RBD residue R498 present in Omicron RBDs. This new salt bridge likely strengthens the interaction with the RBD (**Fig. 6C, E**). Altogether, the structural model of the 2130-1-0114-112 with the BA.2 RBD helps explain the observed restoration of potency against SARS-CoV-2 Omicron VOCs.

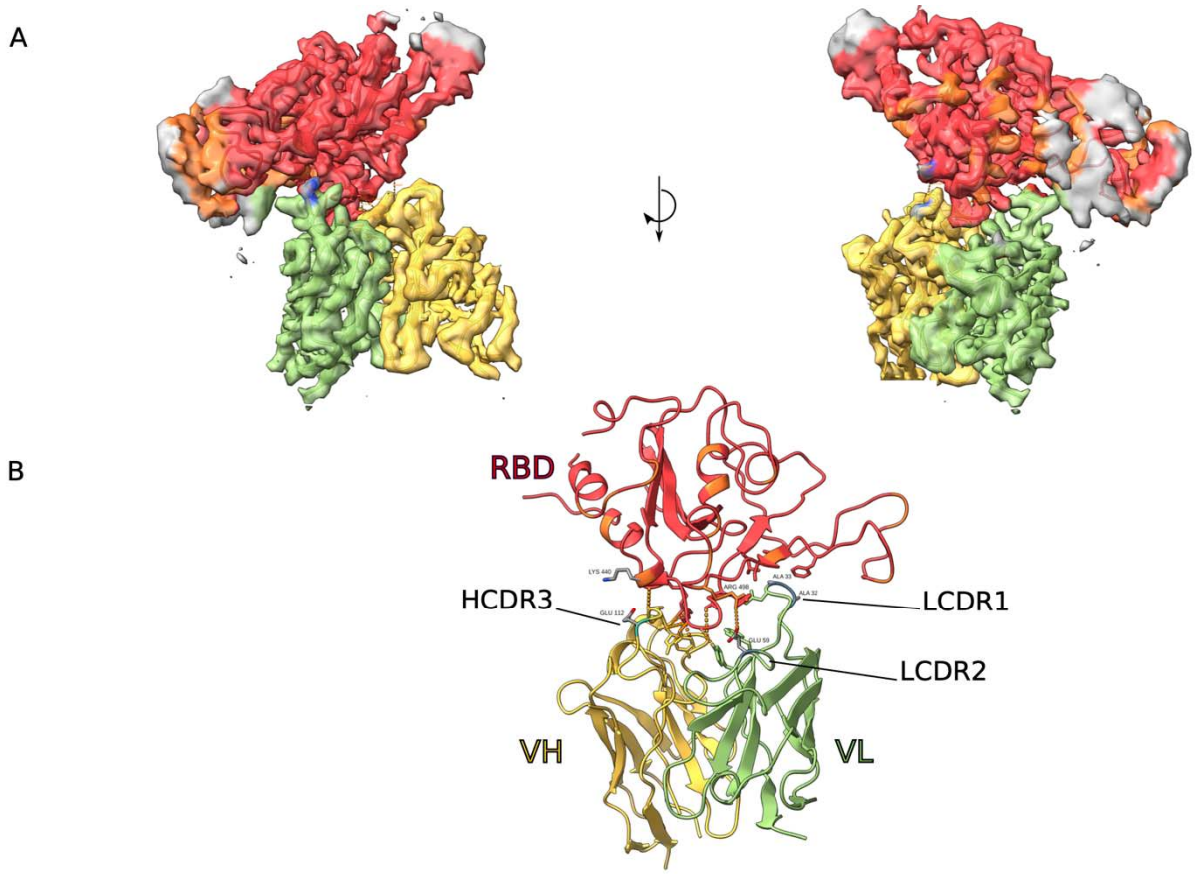

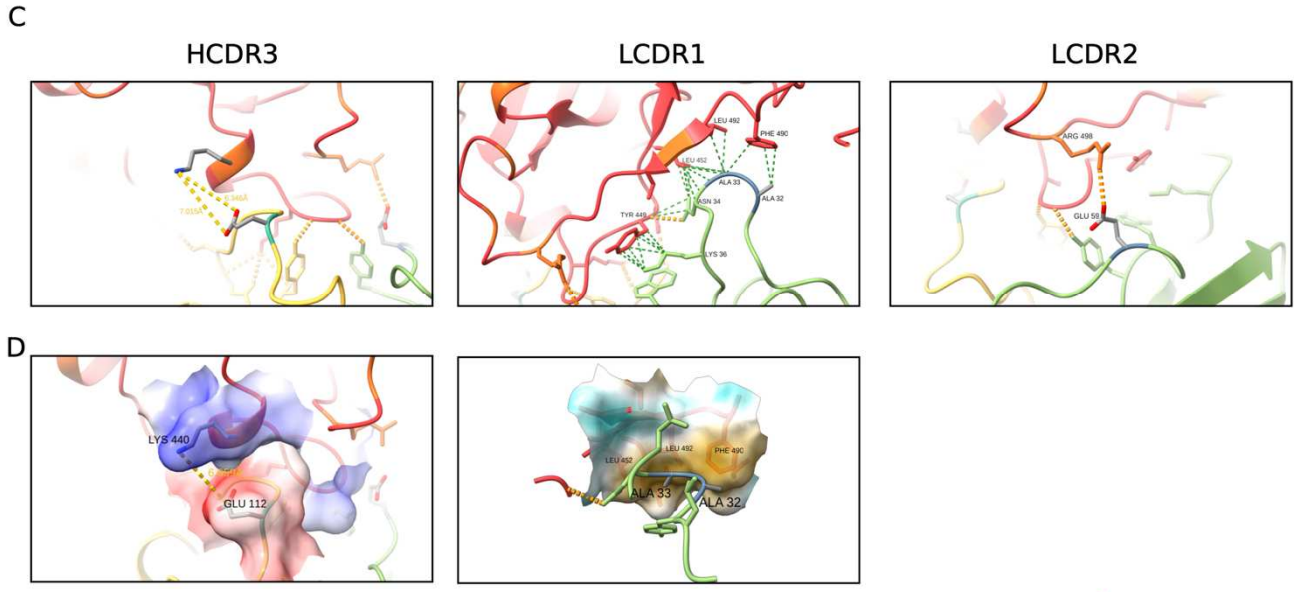

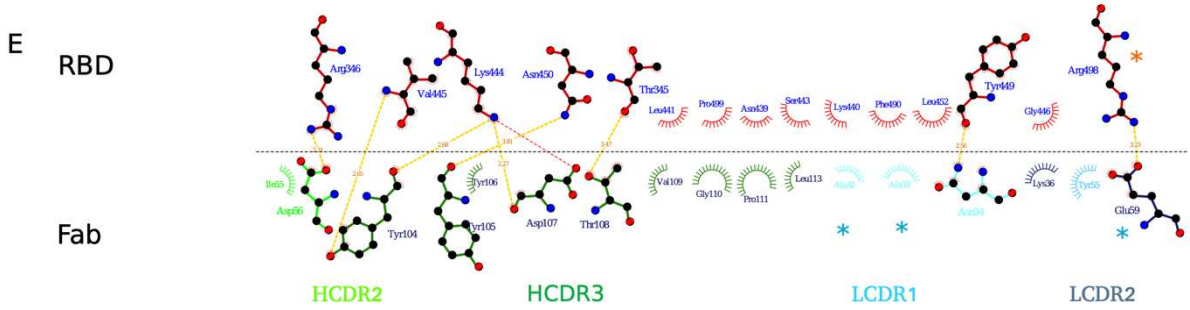

Figure 6: Cryo-EM structure of neutralizing antibodies 2130-1-0114-112 in complex with Cov2 BA.2 RBD. (A) Cryo-EM map and model of the RBD-Fab complex. The map is transparent and colored by chain with RBD red, 2130-1-0114-112 HC yellow and 2130-1-0114-112 LC green. (B) Atomic model of the RBD-Fab complex. Color as in A. Hydrogen bond in dashed line. BA.2 RBD mutation in orange. 2130-1-0114-112 mutation in cyan and blue (HC and LC). (C) Detail showing the 2130-1-0114-112 modified residues and the interaction with Cov2 BA.2 RBD. Left, HCDR3 Glu112. Middle, LCDR1 Ala32 and Ala33 hydrophobic network. Right, LCDR2 Glu59 salt bridge with Arg498. Orange and green dashed lines indicate H-bonds and hydrophobic interactions, respectively; yellow dashed lines are labeled with distances. (D) Left, HCDR3 shown as in (C) with surface color by electrostatic potential, showing the positive and negative charges of Lys444 and Glu112. Right, A32 and A33 in LCDR1 with the nearby RBD surface colored by hydrophobicity (orange to cyan hydrophobic to hydrophilic). (E) 2D diagram of Fab 2130-1-0114-112 paratope and epitope residues involved in hydrogen bonding (dashed lines) and hydrophobic interactions. Residues involved in hydrophobic interactions are shown as curved lines with rays. Atoms shown as circles, with oxygen red, carbon black, and nitrogen blue. Interacting residues that belong to CDR loops are colored in different shade. Asterisks correspond to mutated residues. Image created with Ligplot+ [Laskowski2011].

Discussion:

We set out to rapidly design and validate derivatives of the COV2-2130 antibody that restore potent *in vitro* neutralization against BA.1 and BA.1.1 Omicron subvariants while maintaining binding and neutralization to previous strains of SARS-CoV-2. Additionally, we sought to retain favorable thermostability properties and maintain the sequences' humanness, a data-driven measure of similarity to known human sequences. Despite the multiple mutations in the COV2-2130 epitope of Omicron BA.1 and BA.1.1, we achieved these simultaneous design objectives by applying a scalable, computationally driven, multi-objective approach to design potently neutralizing antibodies against all major SARS-CoV-2 variants. We performed our *in silico* design calculations in a single iteration (i.e., without requiring iterative improvement based on experimental evaluations) in less than 3 weeks. Our top antibody design was confirmed to restore prophylactic efficacy *in vivo* and to also restore strong neutralization of Omicron BA.1 and BA.1.1, while maintaining neutralization of earlier and subsequent VOCs including Delta (B.1.617.2), Omicron BA.2, BA.4, BA.5, and BA.5.5, and also remaining thermostable.

Several designed antibody candidates were successful in restoring neutralization potency to Omicron subvariants. Collectively, these antibodies almost eliminate the significant sequence variation in the CDRH3 loop at positions 103 to 108 present in the initial population of 376 IgG designs (**Fig. ED7**). In contrast, mutations at positions 32 and 33 in CDRL1 appear to be enriched, particularly to hydrophobic residues, consistent with our analysis of this part of the experimentally solved structure of 2130-1-0114-112 and BA.2 spike. As described above, the four designed mutations in this antibody appear to accommodate the mutations in Omicron and optimize both the electrostatic and the hydrophobic interactions with Omicron lineage RBD.

Empirically, this design fully restores potent neutralization against authentic BA.1 and BA.1.1 SARS-CoV-2, while maintaining WA1/2020 D614G and Delta (B.1.617.2) neutralization, meeting our design goals. Indeed, 2130-1-0114-112 had superior antiviral activity *in vivo* against BA.1.1 and BA.5 in susceptible K18-hACE2 mice compared to COV2-2130. Notably, this same antibody design also neutralizes authentic BA.2 and BA.2.12.1; is highly effective against BA.4, against which COV2-2130 suffers a small (< 10-fold) reduction in potency [Wang2022], BA.5, and BA.5.5; and remains potently neutralizing against pseudotyped BA.2.75. These more recent variants, all of which include the Omicron mutations N440K, E484A, and Q498R, had not yet emerged at the time we created our antibody designs, but 2130-1-0114-112's effective neutralization of these VOCs demonstrates the robustness of our multi-objective computational approach and offers hope that future design campaigns may yield designs that also broadly protect against escape mutants. Finally, the parental COV2-2130 suffers a total loss of pseudoviral neutralization against the emerging BA.4.6 subvariant, which contains the mutation R346T, and a constructed BA.2.75 subvariant with the single additional mutation R346T, matching the mutations in BA.2.76 RBD. Against these same subvariants, 2130-1-0114-112 retains some pseudoviral neutralization (IC50 of 1264 and 673.8 ng/ml, respectively). While there is some loss in potency, these activities demonstrate that 2130-1-0114-112's designed mutations can compensate for the loss of the salt bridge from RBD R346 – to heavy chain D56, reducing this vulnerability as compared to COV2-2130.

Our results also show that improvements of more than one order of magnitude in neutralization IC50 values with respect to Omicron BA.1 are possible with as few as two substitutions to the

parental variable region sequence of COV2-2130, as demonstrated by the similar 2130-1-0104-024.

Our computational design methodologies were designed to be rapid, generalizable, and enable rescue of antibodies that suffer loss of potency due to virus escape. In addition to selecting mutant antibody designs based on predicted binding affinity, our approach supports simultaneous consideration and optimization of additional antibody attributes, including putative correlates of manufacturability (thermostability) and/or safety properties (humanness). Importantly, our multi-objective optimization approach simultaneously balances results from multiple affinity prediction models against multiple virus variants and can be tuned to bias the mutational landscape based on investigator design objectives. Importantly, because the computational design process itself is not tied to availability of reagents, survivor serum or lymphocytes, or other lengthy wet laboratory processes, it offers the potential for highly accelerated design or repair of antibody-based drug products.

Critically, our design approach could lead to a quicker path to clinical use, potentially with lower development costs and lower risk as compared to a wholly new drug product screen requiring comparable breadth and efficacy. This is because our top performing antibody restores *in vivo* efficacy and achieves potent and broad neutralization of current SARS-CoV-2 Variants of Concern by substituting only four amino acids into the parental antibody drug product. This parental antibody has previously been extensively tested and already deployed under FDA emergency use authorization. This potentially accelerated path to clinical use is particularly

relevant now, given that traditional antibody drug development approaches are struggling to keep up with the rapid pace of SARS-CoV-2 escape variants.

In future work, we will extend our computational approach to include additional antibody developability predictive models, such as models predicting antibody expression, protein aggregation, and polyreactivity. Our models for predicting antibody-antigen binding heavily depend on performing simulations using accurate models of antibody-antigen co-structures, an important limitation. Consequently, we are developing experimental datasets to advance machine-learning-based approaches for predicting binding directly from sequence, as well as incorporating emerging AI-based approaches for determining and refining structural models.

In summary, we demonstrate critical aspects of a computational antibody design capability and rapidly create hundreds of antibody designs, some of which are potently neutralizing and broadly reactive replacement antibodies for COV2-2130 in the context of Omicron virus subvariants. Similar study of the mutational liabilities of a given antiviral antibody might allow pre-emptive computational design for escape robustness. Ultimately, this computational approach could lead to an on-demand antibody drug product development strategy that would allow for rapid response to emerging viral outbreaks.

References

1. [VanBlargan2022] VanBlargan, L. A. *et al.* An infectious SARS-CoV-2 B.1.1.529 Omicron virus escapes neutralization by therapeutic monoclonal antibodies. *Nat Med* **28**, 490–495 (2022).
2. [Case2022] Case, J. B. *et al.* Resilience of S309 and AZD7442 monoclonal antibody treatments against infection by SARS-CoV-2 Omicron lineage strains. *Nat Commun* **13**, 3824 (2022).
3. [WHO2020] World Health Organization. WHO COVID-19 Dashboard https://covid19.who.int/ (2022).
4. [Wolfel2020] Wölfel, R. *et al.* Virological assessment of hospitalized patients with COVID-2019. *Nature* **581**, 465–469 (2020).
5. [Bai2020] Bai, Y. *et al.* Presumed Asymptomatic Carrier Transmission of COVID-19. *JAMA* **323**, 1406 (2020).
6. [Viana2022] Viana, R. *et al.* Rapid epidemic expansion of the SARS-CoV-2 Omicron variant in southern Africa. *Nature* **603**, 679–686 (2022).
7. [Iketani2022] Iketani, S. *et al.* Antibody evasion properties of SARS-CoV-2 Omicron sublineages. *Nature* **604**, 553–556 (2022).
8. [Wang2022] Wang, Q. *et al.* Antibody evasion by SARS-CoV-2 Omicron subvariants BA.2.12.1, BA.4 and BA.5. *Nature* **608**, 603–608 (2022).
9. [Zost2020] Zost, S. J. *et al.* Potently neutralizing and protective human antibodies against SARS-CoV-2. *Nature* **584**, 443–449 (2020).
10. [Dong2021] Dong, J. *et al.* Genetic and structural basis for SARS-CoV-2 variant neutralization by a two-antibody cocktail. *Nat Microbiol* **6**, 1233–1244 (2021).
11. [Cameroni2022] Cameroni, E. *et al.* Broadly neutralizing antibodies overcome SARS-CoV-2 Omicron antigenic shift. *Nature* **602**, 664–670 (2022).
12. [Tuekprakhon2022] Tuekprakhon, A. *et al.* Antibody escape of SARS-CoV-2 Omicron BA.4 and BA.5 from vaccine and BA.1 serum. *Cell* **185**, 2422-2433.e13 (2022).
13. [Takashita2022] Takashita, E. *et al.* Efficacy of Antibodies and Antiviral Drugs against Omicron BA.2.12.1, BA.4, and BA.5 Subvariants. *N Engl J Med* **387**, 468–470 (2022).
14. [zemla2005] Zemla, A. *et al.* AS2TS system for protein structure modeling and analysis. *Nucleic Acids Research* **33**, W111–W115 (2005).

15. [Mannar2022] Mannar, D. *et al.* SARS-CoV-2 Omicron variant: Antibody evasion and cryo-EM structure of spike protein–ACE2 complex. *Science* **375**, 760–764 (2022).

16. [selaculang2013] Sela-Culang, I., Kunik, V. & Ofran, Y. The Structural Basis of Antibody-Antigen Recognition. *Front. Immunol.* **4**, (2013).

17. [zemla2022] Zemla, A. *et al. SARS-COV-2 Omicron variant predicted to exhibit higher affinity to ACE-2 receptor and lower affinity to a large range of neutralizing antibodies, using a rapid computational platform*. http://biorxiv.org/lookup/doi/10.1101/2021.12.16.472843 (2021) doi:10.1101/2021.12.16.472843.

18. [barlow2018] Barlow, K. A. *et al.* Flex ddG: Rosetta Ensemble-Based Estimation of Changes in Protein–Protein Binding Affinity upon Mutation. *J. Phys. Chem. B* **122**, 5389–5399 (2018).

19. [zhu2022] Zhu, F. *et al.* Large-scale application of free energy perturbation calculations for antibody design. *Sci Rep* **12**, 12489 (2022).

20. [Vashchenko2022] Vashchenko, D. *et al. AbBERT: Learning Antibody Humanness via Masked Language Modeling*. http://biorxiv.org/lookup/doi/10.1101/2022.08.02.502236 (2022) doi:10.1101/2022.08.02.502236.

21. [Olsen2022] Olsen, T. H., Boyles, F. & Deane, C. M. Observed Antibody Space: A diverse database of cleaned, annotated, and translated unpaired and paired antibody sequences. *Protein Science* **31**, 141–146 (2022).

22. [ehrgott2005] Efficiency and Nondominance. in *Multicriteria Optimization* (ed. Ehrgott, M.) 23–64 (Springer, 2005). doi:10.1007/3-540-27659-9_2.

23. [pinto2020] Pinto, D. *et al.* Cross-neutralization of SARS-CoV-2 by a human monoclonal SARS-CoV antibody. *Nature* **583**, 290–295 (2020).

24. [Halfmann2022] Halfmann, P. J. *et al.* SARS-CoV-2 Omicron virus causes attenuated disease in mice and hamsters. *Nature* **603**, 687–692 (2022).

25. [Uraki2022] Uraki, R. *et al.* Characterization and antiviral susceptibility of SARS-CoV-2 Omicron BA.2. *Nature* **607**, 119–127 (2022).

26. [Ying2022] Ying, B. *et al.* Boosting with variant-matched or historical mRNA vaccines protects against Omicron infection in mice. *Cell* **185**, 1572-1587.e11 (2022).

27. [Chen2021] Chen, R. E. *et al*. Resistance of SARS-CoV-2 variants to neutralization by monoclonal and serum-derived polyclonal antibodies. *Nat Med* **27**, 717–726 (2021).
28. [Laskowski2011] Laskowski, R. A. & Swindells, M. B. LigPlot+: Multiple Ligand–Protein Interaction Diagrams for Drug Discovery. *J. Chem. Inf. Model.* **51**, 2778–2786 (2011).

Methods

Modeling and selection of antibody-antigen structures to enable structure-based simulation-based prediction. To best manage the high sensitivity of ddG predictions to structure quality [Geng2019], we used LGA [Zemla2003] to evaluate a collection of experimentally-solved structures of the receptor binding domains (RBD), available structures of the Fab form of COV2-2130, and structures of RBD-Fab complexes to identify regions of backbone and side-chain deviation (see **Fig. ED8**).

We used the conformational centroid for further analysis and to select a representative structure. Structural clustering of tested RBDs identified Omicron RBD (PDB id 7t9k, chain A) as the centroid of all evaluated conformations (shown on **Fig. ED9A**). We consequently chose to perform binding affinity (ddG) calculations on two initial structures (**Fig. ED9B**): an experimentally solved structure of WT RBD with the Fab form of COV2-2130 (PDB ID 7l7e, chains S, M, N); and a structural model of Omicron RBD complexed with COV2-2130 (PDB ID 7l7e, chains M, N) that uses as RBD the identified conformational centroid (PDB ID 7t9k chain A).

Atomistic molecular dynamics (MD) simulations for free-energies as affinity predictions. MD simulations were performed using OpenMM (v7.4) [Eastman2017] and CHARMM36

[Huang2013]. Complexes were first solvated in an isotropic TIP3P [3] box. K^+ and CL^- ions were added to neutrality and 150 mM concentration. After energy minimization, MD simulations with a Langevin integrator (1 ps^{-1}) [Salomon-Ferrer2013], Monte Carlo barostat (303.15 K), particle mesh ewald summation (1 Å grid) [Darden1993], SHAKE [Ryckaert1977], and 2 fs timestep were run for 125 ps with constraints on backbone and sidechain atoms (400 and 40 kJ/mol·nm^2, respectively). An additional 10 ns were run without constraints. From the final coordinates, a minimum watershell [Ovchinnikov2020] with adaptive boundary and hydrogen repartitioning was next used to increase sampling. These simulations used a 4 fs time step [Hopkins2015], 300K thermostat, and particle mesh ewald electrostatics. The antibody and antigen were separated from each other by 8 Å, with separate simulations under harmonic constraints (100 kcal/mol·$Å^2$) at each 1 Å interval. At each, 4 ns of re-equilibration and an additional 360 ns of MD were run to provide sampling for calculating the free-energy [Ovchinnikov2016].

Structural Fluctuation Estimation (SFE) approach for reproducible and robust free energy prediction. To address problems of reproducibility and robustness of calculated estimates in energy changes upon mutations (ddG), we have applied our Structural Fluctuation Estimation (SFE) approach [zemla2022]. The construction of models, clustering, and selection of representatives of each cluster (its centroid) for further processing are described previously in Section “Modeling and selection of antibody-antigen structures to enable structure-based simulation-based predictions”. These structures are minimized and relaxed using standard minimization procedures from Rosetta [Rohl2004], Chimera [Pettersen2004], and GROMACS [Abraham2015] steepest descent and conjugate gradient methods, followed by further short MD

simulations in GROMACS to extract from the resulting trajectories a set of structure snapshots. For each initial structure we generate 60 structural conformations for the RBD-Fab complex (30 complexes with and 30 without mutations where each set of 30 includes the initial structure, four minimized and 25 structures from MD trajectories), capturing structural uncertainties, possible structural deviations upon introduced mutations, and protein natural structural fluctuations. Next, we perform "forward" (on models without mutations) and "reverse" (on models with mutations) mutational ddG calculations using Rosetta Flex ddG [barlow2018]. When ddG calculations are completed we remove outliers, average results of the interquartile simulations, and calculate the final ddG as estimated by the formula: $ddG=(ddG_{forward} - ddG_{reverse})/2$. The resulting ddG value provides an affinity estimate that has been shown to be more reproducible and robust than ddG estimates calculated from just one initial input structure of the RBD-FAB complex using standard FoldX [Schymkowitz2005], Rosetta [Kortemme2002], or Flex ddG [barlow2018] procedures.

AbBERT deep language model. AbBERT [Vashchenko22] is a transformer-based language model we derived from ProtBERT [Elnaggar2021] through fine-tuning the pre-trained model on over 200,000 human antibody sequences from the Observed Antibody Space (OAS) [Olsen2022]. The trained AbBERT model then learns the distribution of human sequences. This provides a way to measure the resemblance of candidate antibodies to human antibodies. We score the effect of single or multiple mutational changes, where the latter is via a multi-unmask scoring procedure. We use these scores in online sequence generation and in post-campaign Pareto selection. As shown in **Fig. ED10**, we can also sample from the model when conditioning on partial sequences.

Free energy perturbation calculations. Free energy perturbation (FEP) is a rigorous, physics-based method that employs MD simulations to calculate free energy differences. As reported recently [zhu2022], we implemented an automated protocol for large-scale FEP calculations to evaluate the effect of antibody mutation on conformational stability. The structure of the COV2-2130 Fab was taken from the crystal structure 7L7E. We then followed the FEP protocol described in Ref. [zhu2022]. Using FEP, we calculated $\Delta\Delta G^{Stability}$, the change in the antibody conformational stability, for 512 single mutations of 29 residues on the COV2-2130 Fab near the binding interface.

Active learning and autonomous system. We employed a semi-autonomous system to select and administer Rosetta Flex [barlow2018] and FoldX [Schymkowitz2005] simulations, broadly exploring and optimizing for binding to BA.1, BA.1.1, and the RBD mutant L452R (the relevant Delta constituent). We treated the set of sequences around COV2-2130, out to 9 mutations difference (mode 4, mean 4.56). Our system coordinates hundreds of individually-scheduled, asynchronously-operating HPC nodes that execute these simulations using HPC workflow design tools [gitMaestro, gitSina]. Each result is recorded in a MariaDB database, which also serves these results to nodes for decision-making. We pre-loaded our database with sequences generated during a pre-Omicron simulation effort to improve COV2-2130's robustness to escape. We selected simulations by both (1) model-free, rules-based, rank-and-select approaches and (2) Gaussian process-based active learning with an MEI decision rule [Mockus1978], with models implemented in GPyTorch [Gardner2018]. In either case, we created the decision set using a

randomized sequence generator. This generator was biased toward individual mutations favored by available results from the in silico estimators and simulators described previously.

Following this phase, we prepared a unified view of the designs. All sequences were scored with the AbBERT model. We next determined the Pareto (non-dominated) set of designs. For each design in this set, we then summed weighted terms from: binding ddG values under Rosetta Flex and FoldX (where present); summed point-mutation binding free energies from pulling simulations; FEP stability estimates; multi- or summed single-point SFE binding free energies; the square of the number of mutations (preferring fewer); and the score from AbBERT. This sum was used as a single score to order the antibody sequences as a ranked set. From this ranked set we first chose the top sequences for antibody production. We then enforced sequence diversity of the selected antibodies for production by limiting the number of times any single point mutation could appear in the overall set by eliminating the lowest ranked antibodies once the maximum was reached. We further enforced sequence diversity by ensuring that the selected set included at least one antibody sequence containing each of the top performing single point mutations based on an exhaustive set of simulations of all single point mutations on the antibody's paratope. In addition, we enforced inclusion of previously unaddressed single point mutations and positions that appeared significant relative to our initial specification of the design problem. We did both by replacing the lowest ranked antibody sequences in the selected set with the top ranked antibody sequences containing top single point mutations not yet represented in the set. Finally, we manually removed any antibody sequences containing more than four mutations to aromatic amino acids and sequence motifs associated with glycosylation.

Antigen production. To express the RBD subdomain of the SARS-CoV-2 S protein, residues 328–531 were cloned into a mammalian expression vector downstream of an mu-phosphatase signal peptide and upstream of an AviTag and a 8×His tag. Three previously identified stabilizing mutations (Y365F, F392W, V395I) were included in the RBD to enhance stability and yield. For RBD constructs corresponding to the Omicron subvariants, mutations present in each subvariant were introduced into the context of the stabilized, wild-type RBD construct. RBD constructs were transfected into Expi293F cells (ThermoFisher Scientific), and expressed protein was isolated by metal affinity chromatography on HisTrap Excel columns (Cytiva). Purified proteins were analyzed by SDS–PAGE to ensure purity and appropriate molecular weights.

Antibody production. Nucleotide sequences encoding the designed heavy and light chain sequences for each antibody in the first set of 230 designs were synthesized, cloned into an hIgG1 framework, and used to produce mAbs via transient transfection of HEK293 cells at ATUM (Newark, CA, USA).

For the second set of 204 designs, monoclonal antibody sequences were synthesized (Twist Bioscience) and cloned into an IgG1 monocistronic expression vector (designated as pVVC-mCisK_hG1) [Chng 2015] and expressed either at microscale in transiently transfected ExpiCHO cells [Zost2020a] for screening or at a larger-scale for down-stream assays. Sequences in this group all contain an additional arginine at the beginning of the light chain constant region with respect to sequences expressed in the first set. Larger-scale monoclonal antibody expression was performed by transfecting (30 ml per antibody) CHO cell cultures using the Gibco ExpiCHO

Expression System and protocol for 125ml flasks (Corning) as described by the vendor. Culture supernatants were purified using HiTrap MabSelect SuRe (Cytiva, formerly GE Healthcare Life Sciences) on a 24-column parallel protein chromatography system (Protein BioSolutions). Purified monoclonal antibodies were buffer-exchanged into PBS, and stored at 4□°C until use.

Binding screening and characterization. Immunoassays for screening the first set of 230 designs (**Fig. ED1**) and later characterization were performed on the Gyrolab xPlore instrument (Gyros Protein Technologies) using the Bioaffy 200 discs (Gyros Protein Technologies). The standard manufacturer's immunoassay automated protocol was executed with fluorescence detection set to 0.1% PMT. Assay column washes were performed with in PBS + 0.02% Tween 20 (PBST). Capture antigens were applied to the assay columns at 0.5 to 2.0 μM in PBS. Analyte mAbs were applied to the assay columns diluted in PBST at 1:200 for single-concentration screening or as a serial dilution from 1,000 nM to 0.25 nM for characterization of down-selected candidate antibodies. A secondary detection antibody served as a fluorescent reporter: Alexa Fluor 647 AffiniPure Fab Fragment Goat Anti-Human IgG, Fcγ fragment specific (Jackson ImmunoResearch) diluted to 50-100 nM in RexxipF buffer (Gyros Protein Technologies). Resulting values were fit to a 4PL model or calculated as area under the curve (AUC) using GraphPad Prism software.

Dose-response ELISA binding assays. For screening and characterizing the second set of 204 designs (**Fig. ED2**), wells of 384-well microtiter plates were coated with purified recombinant SARS-CoV-2 RBD proteins at 4 °C overnight at a concentration of 2 mg/mL of antigen. Plates were washed with Dulbecco's phosphate-buffered saline (DPBS) containing 0.05% Tween-20

(DPBS-T) and blocked with 2% bovine serum albumin and 2% normal goat serum in DPBS-T (blocking buffer) for 1 h. mAbs were diluted in 12 three-fold serial dilutions in blocking buffer at a starting concentration of 10 μg/mL. Plates were then washed and mAb dilutions were added and incubated for 1 h. Plates were washed and a goat anti-human IgG conjugated with horseradish peroxidase (HRP) (Southern Biotech, cat. 2014-05, lot L2118-VG00B, 1:5,000 dilution in blocking buffer) and incubated for 1 h. After plates were washed, signal was developed with a 3,3',5,5'-tetramethylbenzidine (TMB) substrate (Thermo Fisher Scientific). Color development was monitored, 1M hydrochloric acid was added to stop the reaction, and the absorbance was measured at 450 nm using a spectrophotometer (Biotek). Dose-response ELISAs were performed in technical triplicate with at least two independent experimental replicates.

Thermal Shift Protein Assays (melt-curve assays). Antibody concentrations were determined using the Qubit Protein Assay Kit (ThermoFisher). The GloMelt™ Thermal Shift Protein Stability Kit (Biotum) was utilized to determine the thermal stability of the antibodies, following the manufacturer's suggested protocols. The analysis was performed using a melt-curve program on an ABI 7500 Fast Dx Real-Time PCR instrument. Each assay was done in triplicates, using 5ug of mAb per well. The raw melt curve data was imported into and analyzed via Protein Thermal Shift ™ software version 1.4 (ThermoFisher) to generate the melting temperature and fit data.

Pseudovirus Neutralization. Pseudovirus neutralization assays were carried out according to the protocol of Crawford *et al*. [VPneut1]. One day prior to the assay, 293T cells stably

expressing human ACE2 (293T-hACE2 cells) were seeded onto 96-well tissue culture plates coated with poly-D-lysine. The day of the assay, serial dilutions of monoclonal antibodies in duplicate were prepared in a 96-well microtiter plate and pre-incubated with pseudovirus for 1 h at 37 °C in the presence of a final concentration of 5 mg/mL polybrene (EMD Millipore), before the pseudovirus-mAb mixtures were added to 293T-hACE2 monolayers. Plates were returned to the 37 °C incubator, and then 48-60 h later luciferase activity was measured on a CLARIOStar plate reader (BMG LabTech) using the Bright-Glo Luciferase Assay System (Promega). Percent inhibition of pseudovirus infection was calculated relative to pseudovirus-only control. IC50 values were determined by nonlinear regression using Prism v.8.1.0 (GraphPad). Each neutralization assay was repeated at least twice.

Viruses. The WA1/2020 recombinant strain with D614G substitution and B.1.617.2 was described previously [Plante2020][Ying2021]. The BA.1 isolate was obtained from an individual in Wisconsin as a mid-turbinate nasal swab [Halfmann2022]. The BA.1.1 and BA.2 strains were obtained from nasopharyngeal isolates. The BA.2.12.1, BA.4, BA.5, and BA.5.5 isolates were generous gifts from M. Suthar (Emory University), A. Pekosz (Johns Hopkins University), and R. Webby (St. Jude Children's Research Hospital). All viruses were passaged once on Vero-TMPRSS2 cells and subjected to next-generation sequencing [Chen2021] to confirm the introduction and stability of substitutions. All virus experiments were performed in an approved biosafety level 3 (BSL-3) facility.

Focus reduction neutralization test. Serial dilutions of sera were incubated with 10^2 focus-forming units (FFU) of WA1/2020 D614G, B.1.617.2, BA.1, BA.1.1, BA.2, BA.2.12.1, BA.4,

BA.5, or BA.5.5 for 1 h at 37°C. Antibody-virus complexes were added to Vero-TMPRSS2 cell monolayers in 96-well plates and incubated at 37°C for 1 h. Subsequently, cells were overlaid with 1% (w/v) methylcellulose in MEM. Plates were harvested 30 h (WA1/2020 D614G and B.1.617.2) or 70 h (BA.1, BA.1.1, BA.2, BA.2.12.1, BA.4, BA.5, and BA.5.5) later by removing overlays and fixed with 4% PFA in PBS for 20 min at room temperature. Plates were washed and sequentially incubated with a pool (SARS2-02, -08, -09, -10, -11, -13, -14, -17, -20, -26, -27, -28, -31, -38, -41, -42, -44, -49, -57, -62, -64, -65, -67, and -71 [VanBlargan2021]) of anti-S murine antibodies (including cross-reactive mAbs to SARS-CoV) and HRP-conjugated goat anti-mouse IgG (Sigma Cat # A8924, RRID: AB_258426) in PBS supplemented with 0.1% saponin and 0.1% bovine serum albumin. SARS-CoV-2-infected cell foci were visualized using TrueBlue peroxidase substrate (KPL) and quantitated on an ImmunoSpot microanalyzer (Cellular Technologies).

Mouse studies. Animal studies were carried out in accordance with the recommendations in the Guide for the Care and Use of Laboratory Animals of the National Institutes of Health. The protocols were approved by the Institutional Animal Care and Use Committee at the Washington University School of Medicine (assurance number A3381–01). Virus inoculations were performed under anesthesia that was induced and maintained with ketamine hydrochloride and xylazine, and all efforts were made to minimize animal suffering.

Heterozygous K18-hACE2 C57BL/6J mice (strain: 2B6.Cg-Tg(K18-ACE2)2Prlmn/J, Cat # 34860) were obtained from The Jackson Laboratory. Animals were housed in groups and fed standard chow diets.

Eight-week-old female K18-hACE2 C57BL/6 mice were administered 100 μg of 2130-1-0114-112, parental 2130, or isotype control anti-West Nile hE16 mAb [Oliphant2005] by intraperitoneal injection one day before intranasal inoculation with with 104 focus-forming units (FFU) of WA1/2020 D614G, BA.1.1 or BA.5. Animals were euthanized at 4 days post-infection and tissues were harvested for virological analysis.

Measurement of Viral RNA burden. Tissues were weighed and homogenized with zirconia beads in a MagNA Lyser instrument (Roche Life Science) in 1 ml of DMEM medium supplemented with 2% heat-inactivated FBS. Tissue homogenates were clarified by centrifugation at 10,000 rpm for 5 min and stored at −80°C. RNA was extracted using the MagMax mirVana Total RNA isolation kit (Thermo Fisher Scientific) on the Kingfisher Flex extraction robot (Thermo Fisher Scientific). RNA was reverse transcribed and amplified using the TaqMan RNA-to-CT 1-Step Kit (Thermo Fisher Scientific). Reverse transcription was carried out at 48°C for 15 min followed by 2 min at 95°C. Amplification was accomplished over 50 cycles as follows: 95°C for 15 s and 60°C for 1 min. Copies of SARS-CoV-2 *N* gene RNA in samples were determined using a published assay [Case2020].

Cryo-EM sample preparation and data collection. The Fab 2130-1-0114-112 and Cov2 BA.2 were expressed recombinantly and combined in a molar ration of 1:4 (Ag:Fab). The mixture was incubated over-night at 4°C and purified by gel filtration. 2.2µl of the purified mixture at concentration of 0.5 mg/mL was applied to glow discharged (30 s at 25mA) grid (300 mesh 1.2/1.3, Quantifoil). The grids were blotted for 3.5 s before plunging into liquid ethane using Vitrobot MK4 (TFS) at 20°C and 100% RH. Grids were screened on a Glacios (TFS) microscope and imaged on Krios operated at 300 keV equipped with a K3 and GIF (Gatan) DED detector using counting mode. Movies were collected at nominal magnification of 130,000X, pixel size of 0.647 Å/pixel and defocus range of 0.8 to 1.8 µm. Grids were exposed at ~1.09 e^- /$Å^2$/frame resulting in total dose of ~52.2 e^-/$Å^2$ (**Table EDT2**).

Cryo-EM data processing. Data processing was performed with Relion 4.0 beta2 [Kimanius2021]. Movies were preprocessed with Relion Motioncor2 [Zheng2017] and CTFFind4 [Rohou2015]. Micrographs with low resolution, high astigmatism and defocus were removed from the data set. The data set was first manual pick to generate 2D images and then autopicked by Relion template picker [Fernandez-Leiro2017] and was subject to 2D and 3D classification. Good classes were selected and used for another round of autopicking with Topaz training and Topaz picking [Bepler2020][Kimanius2021]. The particles were extracted in a box size of 600 pixel and binned to 96 pixels (pixel size of 4.04 Å/pixel). The particles were subjected to multiple rounds of 2D class averages, 3D initial map and 3D classification without symmetry to obtain a clean homogeneous particle set. This set was re-extracted at a pixel size of 1.516 Å/pixel and was subjected to 3D autorefinement. The data were further re-extracted at a pixel size of 1.29Å/pixel and processed with CTFrefine, polished [Zivanov2018] and subjected

to final 3D autorefinement and postprocessing resulting in ~3.26Å map. To better resolve the area of interaction between Cov2-RBD/2130-1-0114-112, a focused refinement was performed by particles expansion (C3 symmetry) and signal subtraction with masking around the RBD/2130-1-0114-112. The subtracted particles were subjected to 3D classification without alignment and selected particles were subjected to 3D autorefinement and postprocessing resulting in ~3.7Å map. Detailed statistics are provided in **Fig. ED6** and **Table EDT2**.

Model building and refinement. For model building PDB: 7L7E [Dong2021] was used for initial modelling of the RBD and the 2130-1-0114-112 Fv. All the models were first docked to the map with Chimera [Pettersen2004] or ChimeraX [Pettersen2021]. To improve the coordinates the models were subjected to iterative refinement of manual building in Coot [Emsley2004] and Phenix [Adams2010][Afonine2018]. The models were validated with Molprobity [Chen2010] (**Table EDT2**). The EM map and model has been deposited into EMDB (EMD-28198, EMD-28199) and PDB (8EDK).

Data availability

The datasets generated during and/or analyzed during the current study are available from the corresponding author on reasonable request. The EM map and model has been deposited into EMDB (EMD-28198, EMD-28199) and PDB (8EDK). Selected sequence records are in the accompanying extended data.

Code availability

Codes may be available upon reasonable request to the corresponding author.

References: Methods

29. [Geng2019] Geng, C., Xue, L. C., Roel-Touris, J. & Bonvin, A. M. J. J. Finding the $\Delta\Delta G$ spot: Are predictors of binding affinity changes upon mutations in protein–protein interactions ready for it? *WIREs Comput Mol Sci* **9**, (2019).
30. [Zemla2003] Zemla, A. LGA: a method for finding 3D similarities in protein structures. *Nucleic Acids Research* **31**, 3370–3374 (2003).
31. [Eastman2017] Eastman, P. *et al.* OpenMM 7: Rapid development of high performance algorithms for molecular dynamics. *PLoS Comput Biol* **13**, e1005659 (2017).
32. [Huang2013] Huang, J. & MacKerell, A. D. CHARMM36 all-atom additive protein force field: Validation based on comparison to NMR data. *J. Comput. Chem.* **34**, 2135–2145 (2013).
33. [Salomon-Ferrer2013] Salomon-Ferrer, R., Götz, A. W., Poole, D., Le Grand, S. & Walker, R. C. Routine Microsecond Molecular Dynamics Simulations with AMBER on GPUs. 2. Explicit Solvent Particle Mesh Ewald. *J. Chem. Theory Comput.* **9**, 3878–3888 (2013).
34. [Darden1993] Darden, T., York, D. & Pedersen, L. Particle mesh Ewald: An $N \cdot \log(N)$ method for Ewald sums in large systems. *The Journal of Chemical Physics* **98**, 10089–10092 (1993).
35. [Ryckaert1977] Ryckaert, J.-P., Ciccotti, G. & Berendsen, H. J. C. Numerical integration of the cartesian equations of motion of a system with constraints: molecular dynamics of n-alkanes. *Journal of Computational Physics* **23**, 327–341 (1977).
36. [Ovchinnikov2020] Ovchinnikov, V., Conti, S., Lau, E. Y., Lightstone, F. C. & Karplus, M. Microsecond Molecular Dynamics Simulations of Proteins Using a Quasi-Equilibrium Solvation Shell Model. *J. Chem. Theory Comput.* **16**, 1866–1881 (2020).
37. [Hopkins2015] Hopkins, C. W., Le Grand, S., Walker, R. C. & Roitberg, A. E. Long-Time-Step Molecular Dynamics through Hydrogen Mass Repartitioning. *J. Chem. Theory Comput.* **11**, 1864–1874 (2015).
38. [Ovchinnikov2016] Ovchinnikov, V., Nam, K. & Karplus, M. A Simple and Accurate Method To Calculate Free Energy Profiles and Reaction Rates from Restrained Molecular Simulations of Diffusive Processes. *J. Phys. Chem. B* **120**, 8457–8472 (2016).
39. [Rohl2004] Rohl, C. A., Strauss, C. E. M., Chivian, D. & Baker, D. Modeling structurally variable regions in homologous proteins with rosetta. *Proteins* **55**, 656–677 (2004).
40. [Pettersen2004] Pettersen, E. F. *et al.* UCSF Chimera-A visualization system for exploratory research and analysis. *J. Comput. Chem.* **25**, 1605–1612 (2004).
41. [Abraham2015] Abraham, M. J. *et al.* GROMACS: High performance molecular simulations through multi-level parallelism from laptops to supercomputers. *SoftwareX* **1–2**, 19–25 (2015).
42. [Schymkowitz2005] Schymkowitz, J. *et al.* The FoldX web server: an online force field. *Nucleic Acids Research* **33**, W382–W388 (2005).
43. [Kortemme2002] Kortemme, T. & Baker, D. A simple physical model for binding energy hot spots in protein–protein complexes. *Proc. Natl. Acad. Sci. U.S.A.* **99**, 14116–14121 (2002).
44. [Elnaggar2021] Elnaggar, A. *et al.* ProtTrans: Towards Cracking the Language of Lifes Code Through Self-Supervised Deep Learning and High Performance Computing. *IEEE Trans. Pattern Anal. Mach. Intell.* 1–1 (2021) doi:10.1109/TPAMI.2021.3095381.
45. [gitMaestro] Di Natale, F. et al. Maestro Workflow Conductor https://github.com/LLNL/maestrowf (2022).
46. [gitSina] Haluska, R. et al. Sina https://github.com/LLNL/Sina (2022).
47. [Mockus1978] Mockus, J., Tiesis, V., and Zilinskas A. The application of Bayesian methods for seeking the extremum. *Towards global optimization*, **2**, 117-129 (1978).
48. [Gardner2018] Gardner, J. R., Pleiss, G., Bindel, D., Weinberger, K. Q. & Wilson, A. G. GPyTorch: Blackbox Matrix-Matrix Gaussian Process Inference with GPU Acceleration. Preprint at http://arxiv.org/abs/1809.11165 (2021).
49. [Chng 2015] Chng, J. *et al.* Cleavage efficient 2A peptides for high level monoclonal antibody expression in CHO cells. *mAbs* **7**, 403–412 (2015).

50. [Zost2020a] Zost, S. J. *et al.* Rapid isolation and profiling of a diverse panel of human monoclonal antibodies targeting the SARS-CoV-2 spike protein. *Nat Med* **26**, 1422–1427 (2020).
51. [VPneut1] Crawford, K. H. D. *et al.* Protocol and Reagents for Pseudotyping Lentiviral Particles with SARS-CoV-2 Spike Protein for Neutralization Assays. *Viruses* **12**, 513 (2020).
52. [VanBlargan2021] VanBlargan, L. A. *et al.* A potently neutralizing SARS-CoV-2 antibody inhibits variants of concern by utilizing unique binding residues in a highly conserved epitope. *Immunity* **54**, 2399-2416.e6 (2021).
53. [Plante2020] Plante, J. A. *et al.* Spike mutation D614G alters SARS-CoV-2 fitness. *Nature* **592**, 116–121 (2021).
54. [Ying2021] Ying, B. *et al. Protective activity of mRNA vaccines against ancestral and variant SARS-CoV-2 strains*. http://biorxiv.org/lookup/doi/10.1101/2021.08.25.457693 (2021) doi:10.1101/2021.08.25.457693.
55. [Oliphant2005] Oliphant, T. *et al.* Development of a humanized monoclonal antibody with therapeutic potential against West Nile virus. *Nat Med* **11**, 522–530 (2005).
56. [Case2020] Case, J. B., Bailey, A. L., Kim, A. S., Chen, R. E. & Diamond, M. S. Growth, detection, quantification, and inactivation of SARS-CoV-2. *Virology* **548**, 39–48 (2020).
57. [Kimanius2021] Kimanius, D., Dong, L., Sharov, G., Nakane, T. & Scheres, S. H. W. New tools for automated cryo-EM single-particle analysis in RELION-4.0. *Biochemical Journal* **478**, 4169–4185 (2021).
58. [Zheng2017] Zheng, S. Q. *et al.* MotionCor2: anisotropic correction of beam-induced motion for improved cryo-electron microscopy. *Nat Methods* **14**, 331–332 (2017).
59. [Rohou2015] Rohou, A. & Grigorieff, N. CTFFIND4: Fast and accurate defocus estimation from electron micrographs. *Journal of Structural Biology* **192**, 216–221 (2015).
60. [Fernandez-Leiro2017] Fernandez-Leiro, R. & Scheres, S. H. W. A pipeline approach to single-particle processing in *RELION*. *Acta Crystallogr D Struct Biol* **73**, 496–502 (2017).
61. [Bepler2020] Bepler, T., Kelley, K., Noble, A. J. & Berger, B. Topaz-Denoise: general deep denoising models for cryoEM and cryoET. *Nat Commun* **11**, 5208 (2020).
62. [Zivanov2018] Zivanov, J. *et al.* New tools for automated high-resolution cryo-EM structure determination in RELION-3. *eLife* **7**, e42166 (2018).
63. [Pettersen2021] Pettersen, E. F. *et al.* UCSF ChimeraX: Structure visualization for researchers, educators, and developers. *Protein Science* **30**, 70–82 (2021).
64. [Emsley2004] Emsley, P. & Cowtan, K. *Coot*: model-building tools for molecular graphics. *Acta Crystallogr D Biol Crystallogr* **60**, 2126–2132 (2004).
65. [Adams2010] Adams, P. D. *et al. PHENIX*: a comprehensive Python-based system for macromolecular structure solution. *Acta Crystallogr D Biol Crystallogr* **66**, 213–221 (2010).
66. [Afonine2018] Afonine, P. V. *et al.* Real-space refinement in *PHENIX* for cryo-EM and crystallography. *Acta Crystallogr D Struct Biol* **74**, 531–544 (2018).
67. [Chen2010] Chen, V. B. *et al. MolProbity*: all-atom structure validation for macromolecular crystallography. *Acta Crystallogr D Biol Crystallogr* **66**, 12–21 (2010).

Acknowledgements

This work was performed under the auspices of the U.S. Department of Energy by Lawrence Livermore National Laboratory (LLNL) under contract DE-AC52-07NA27344. The work was supported by the DOD's Joint Program Executive Office for Chemical, Biological, Radiological

and Nuclear Defense, in collaboration with the Defense Health Agency COVID funding initiative under agreement 11647302 in support of the Generative Unconstrained Intelligent Drug Engineering (GUIDE) program (Christopher Earnhart), the Defense Advanced Research Projects Agency (DARPA) agreement number HR0011154580 (Amy Jenkins), Laboratory Directed Research and Development programs (20-ERD-032 and 20-ERD-064) at LLNL., and grants and contracts from the NIH (R01 AI157155, NIAID Centers of Excellence for Influenza Research and Response (CEIRR) contract 75N93019C00051). EM data collections were conducted at the Center for Structural Biology Cryo-EM Facility at Vanderbilt University. The authors wish to thank Christopher Earnhart, Svetlana Hopkins, Amy Jenkins, and Jim Brase for significant technical and programmatic contributions and for facilitating this collaborative research effort. The authors also thank the labs of Prof Sriram Subramaniam and Prof Xinquan Wang for their CryoEM structures of Omicron ahead of release.

LLNL-JRNL-839587-DRAFT.

Contribution Statement

TAD, KTA, ATZ, EYL, FZ, SC, SZ, EB, LBT, BWS, AML, SS, MSD, JEC, RHC, and DMF contributed to the conception or design of the study. TAD, KTA, DR, SC, SZ, EB, EMS, TBE, EC, DRW, JK-YL, BR, EAS, TW, T-HL, BW, JBC, EAG, BKP, LBT, BWS, MSD, JEC, RHC, and DMF acquired, analyzed, or interpreted data. TAD, ATZ, EYL, FZ, JWG, DV, SN, AL, MSS, RMH, EAG, BKP, and DMF created new software. TAD, KTA, ATZ, EYL, FZ, DR, SC, SZ, EB, TE, TWB, BKP, BWS, MSD, JEC, RHC, and DMF drafted or substantively revised the manuscript.

COMPETING FINANCIAL INTERESTS

M.S.D. is a consultant for Inbios, Vir Biotechnology, Senda Biosciences, Moderna and Immunome. The Diamond laboratory has received unrelated funding support in sponsored research agreements from Moderna, Vir Biotechnology, and Emergent BioSolutions. J.E.C. has served as a consultant for Luna Labs USA, Merck Sharp & Dohme Corporation, Emergent Biosolutions, and GlaxoSmithKline, is a member of the Scientific Advisory Board of Meissa Vaccines, a former member of the Scientific Advisory Board of Gigagen (Grifols) and is founder of IDBiologics. The laboratory of J.E.C. received unrelated sponsored research agreements from AstraZeneca, Takeda, and IDBiologics during the conduct of the study. Lawrence Livermore National Laboratory, Los Alamos National Laboratory, and Vanderbilt University have applied for patents for some of the antibodies in this paper, for which T.A.D, A.T.Z., E.Y.L., F.Z., A.M.L., R.H.C., J.E.C., and D.M.F. are inventors. Vanderbilt University has licensed certain rights to antibodies in this paper to Astra Zeneca.

Supplementary Information is available for this paper.

Correspondence and requests for materials should be addressed to D.M.F.